Long-range helium excimer potentials ($A, C^1\Sigma^+_{u,g}$ and $a, c^3\Sigma^+_{u,g}$) from high-resolution differential cross sections for $He(2^1S, 2^3S) + He$

Bernhard Brutschy and Hellmut Haberland
Fakultät für Physik der Universität Freiburg, Freiburg, Germany
(Received 9 May 1978)

The long-range parts of the $A, C\,^1\Sigma^+_{u,g}$ and $a, c\,^3\Sigma^+_{u,g}$ excimer potentials of the He_2 molecule have been accurately determined from high-resolution differential-cross-section measurements in the relative kinetic-energy range from 18 to 140 meV. The barrier heights and internuclear distances of the intermediate maxima of the A and the a state have been obtained with an accuracy of better than 2–5 meV and 0.1 Å, respectively. The long-range parts of the singlet potentials from the *ab initio* calculation by Gubermann and Goddard are always 5–20 meV higher than the potential determined from our experiments, but the splitting of the potentials coincides with our results within experimental accuracy for $R \geq 3$ Å. The experimental set-up, data evaluation, and the construction of the potential are described in detail. The complicated interference structure of the angular distribution is discussed with the help of the quantal deflection function. Total and excitation-transfer cross sections are calculated and compared to other experimental results, and the similarity to other exchange processes is pointed out.

I. INTRODUCTION

The helium atom has two metastable states ($1s2s, 2\,^1S$) and ($1s2s, 2\,^3S$), both separated by roughly 20 eV from the $1s^2$ ground state. These states live long enough to be practically stable for usual experimental conditions, and can be easily detected because of their large excitation energy. Numerous experiments have been performed with atoms in these metastable states. They play an important role in gas discharges[1] and lasers[2]; they have been studied by optical pumping,[3] absorption and emission,[1,4] Penning ionization,[5,6] and by stationary and flowing afterglows.[1,6] They build bubbles in liquid helium,[7] and their excitation energy can be used to operate continuum vacuum-ultraviolet-light sources.[8] Spontaneous anti-Stokes light scattering from them has recently been proposed by Harris[9] to build a tunable incoherent light source that might be 10^3 times more intense than the standard He resonance line sources.

Most of these experiments need, for a reliable interpretation, some knowledge of the interaction potential between a He* atom and a ground-state He atom. The excited He_2 potentials have first been calculated by Buckingham and Dalgarno[10] and subsequently by many other authors.[11] These potentials are very unusual. They have deep (~2 eV) chemical minima at an internuclear distance R of ~1 Å, intermediate maxima at $R \approx 3$ Å, and very shallow (<0.001 eV) Van der Waals minima at very large R(>6 Å).

We have performed differential cross-section measurements for the He*-He system in the energy range from 18 to 140 meV, and have extracted from the data reliable long-range interaction potentials for both spin states. Together with the short-range potentials of other authors, the lowest excimer potentials have been determined completely.

II. EXPERIMENT

A. Principle of the experiment

Two beams of ground-state helium atoms are generated as shown in Fig. 1. Atoms in one beam are excited by electron impact to many electronically excited states, all of which decay but the two metastable ($1s2s, 2\,^1S$) and ($1s2s, 2\,^3S$) states. The singlet state can be quenched optically:

$$\begin{aligned} He(2\,^1S) + h\nu(2059\text{ nm}) &\rightarrow He(2\,^1P) \\ &\rightarrow He(2\,^1S) + h\nu(2059\text{ nm}) \\ &\rightarrow He(1\,^1S) + h\nu(58,4\text{ nm}). \end{aligned}$$

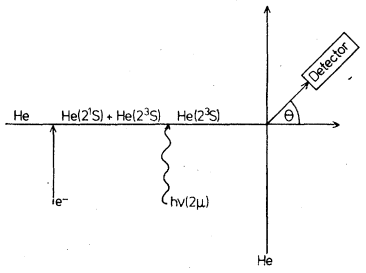

FIG. 1. Principle of the experiment. A beam of He atoms is excited by electron impact to the two metastable states. Atoms in the $He(2\,^1S)$ state can be optically quenched by the 2μ radiation. The beam of excited He atoms is scattered by a beam of ground-state He atoms, and electronically excited particles are detected on the detector.

TABLE I. Energy, lifetimes, and decay modes of the three lowest excited states of the He atom.

He state	Energy (eV)	Lifetime	Decay mode
He($2\,^3S$)	19.82	$\sim 10^3$ sec	$M1$
He($2\,^1S$)	20.61	19.5 msec	$2E1$
He($2\,^1P$)	21.21	2 nsec	$E1$

Only every thousandth atoms decays back to the metastable state, which can therefore be depopulated very efficiently. The two beams are crossed at a right angle and electronically excited particles are detected at some scattering angle θ. Table I compares the energies, lifetimes, and decay modes of the metastable states to the values of the $2P$ state, which can decay via an optically allowed transition.

B. Beam production

Interference patterns of angular distributions can be easily washed out by insufficient resolution. Therefore the ground-state beams are generated by two supersonic nozzle sources operating at very high pressures and a small nozzle that gives beams with narrow velocity spreads. The kinetic energy of an atomic beam leaving a supersonic nozzle is given by $\frac{5}{2}kT$, where T is the temperature of the gas before the expansion. Two different beam sources were used, depending on the energy range desired. One which could be used between 80 and 300 K is shown schematically in Fig. 2. The other operated between 300 and 1600 K, giving an accessible energy range of 16–300 meV. The typical inlet pressure is 20 bar at the lower temperature and 100 bar at the higher one. The beam sources are pumped by unbaffled 10″ diffusion pumps having a 7000-l/sec pumping speed for helium. By operating a Roots blower between diffusion and forepump, the diffusion pump could be operated up to 3×10^{-3} Torr, giving a throughput of 21 Torr liter/sec.

The central part of both beams passes through Campargue-type skimmers.[12] The ground-state beam is mechanically modulated and collimated to 0.4° before the collision center. The other beam enters a second differential pumping chamber, which contains the electron gun, electromagnet, and quench lamp.

An analysis of the excitation of a He atom by electron impact has shown[13] that the good velocity resolution can best be preserved if electron and atomic beams move parallel or antiparallel. Figure 2 shows the parallel configuration. Electrons are emitted by an indirectly heated sinter cathode, which has a spherical electron emitting surface

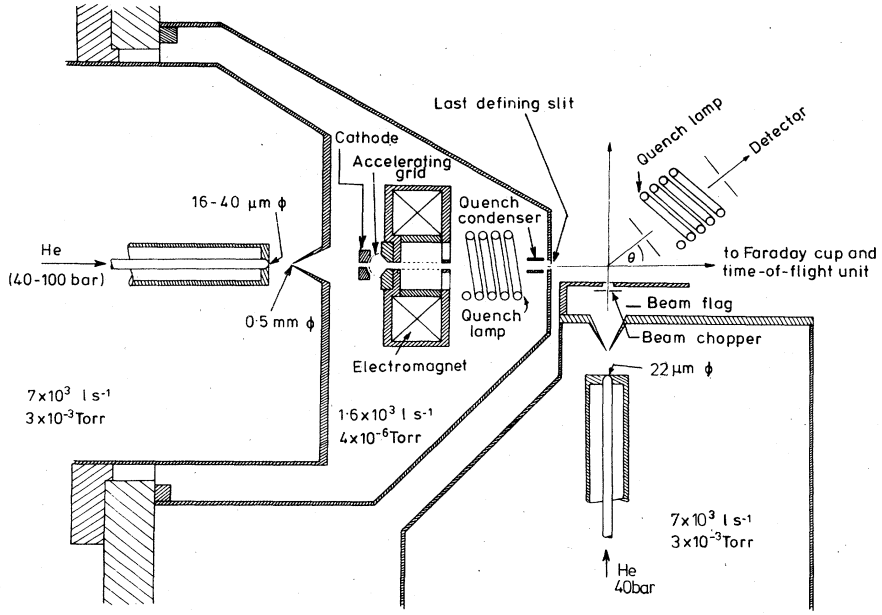

FIG. 2. Central part of the apparatus. The two He beams are generated by two supersonic nozzles of variable temperature. The electrons are emitted by a spherical cathode and are accelerated by a concentric grid. The He beam passes through the hole in the cathode and is excited in the electromagnet. Both beams are collimated to 0.4°, and the excited particles are detected by their electron emission on the first dynode of an open electron multiplier.

and a hole at its center for the passage of the beam. The electrons are accelerated by a spherical net and collide with the helium beam in the electromagnet (~600 G), whose field compensates the diverging effects of the electron space charge. The electron voltage and current are typically 200 V and 30 mA, respectively.

The quenchlamp is wound helically around the beam. For kinetic energies above 100 meV, a single lamp was found not to be sufficient for complete (~99.5%) quenching efficiency. A second quenchlamp installed in front of the detector was used in this case. The quenching efficiencies were checked by measuring the Penning electron spectra of He*-Ar collisions.[35]

The He* beam is also collimated to 0.4°, and has an intensity of roughly 10^{10} He*/sec, of which about $\frac{1}{6}$ is in the triplet state. The intensity of the ground-state beam is six to seven orders of magnitude larger. The electron beam excites approximately only every thousandth atom to the metastable state. But only ~10^{-4} of the excited He atoms remain in the beam. All others are scattered out of the beam by the excitation process and hit some collimating diaphragms before entering the collision chamber.[13]

C. Velocity distributions

The velocity distributions of both beams can be observed by the time-of-flight (TOF) method. The beams are mechanically chopped at the entrance of two long TOF tubes, and the TOF spectra are recorded by a very fast multiscaler. The ground-state beam is excited by electron impact to its metastable states directly behind the chopper, so that it can be detected easily without a mass spectrometer. Figure 3 shows some velocity distributions of the He* beam. The data show a double-peaked structure for flight times longer than 0.5 ms. The peak at smaller flight times is due to He* atoms of the primary excitation process[13]:

$$\mathrm{He} + e^- \rightarrow \mathrm{He}^* + e^- .$$

The second peak, at larger flight times, which has exactly the velocity of the unexcited helium beam, is due to a subsequent resonant energy transfer

$$\mathrm{He}^* + \mathrm{He} \rightarrow \mathrm{He} + \mathrm{He}^* .$$

The difference in flight times between the two peaks is caused by the momentum transfer of the

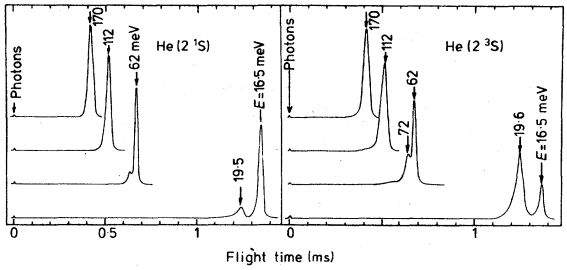

FIG. 3. Time-of-flight distributions. The double-peaked structures result from the momentum transfer by the electron during the excitation process.

electron to the helium atom during the excitation process. The cross section for the resonant energy transfer process is in a first approximation proportional to the g-u splitting of the two corresponding excited-state potential curves of the He_2 molecule.[1] The Van der Waals constants for the singlet state differ by 10%, while they are equal for the triplet state.[17] This leads to a larger splitting and therefore an increased rate of energy transfer and a better velocity resolution of the singlet He* beams. A more detailed analysis of the velocity spectra has been published elsewhere.[13] A simple calculation shows that more than 98% of the excitation-transfer collisions occur before the beam crosses the scattering center, so that Fig. 3 shows the relevant velocity distributions.

D. Beam detection

The metastable atoms are detected by their electron emission on the first dynode of an electron multiplier. The probability for electron emission has been measured absolutely by Rundel *et al.*[14] The emission probability depends on the material of the detector, its gas coverage, and its past history. It is universally assumed that the emission probability is independent of the kinetic energy of the excited atom. To check this assumption, the differential cross section for scattering of He($2\,^1S$) from He was measured twice at the same center of mass energy ($E = 42$ meV), but under different laboratory conditions. One of the two beams was alternatively cooled to the temperature of liquid nitrogen, the other one left at room temperature.

Figure 4 shows the two velocity vector or Newton diagrams[15] for the two runs. The velocity of the He* impinging on the surface of the detector changes by a factor of 2.2. The largest energy ($E = 86$ meV) is obtained for $\theta_{\mathrm{lab}} = 45°$. Figure 5

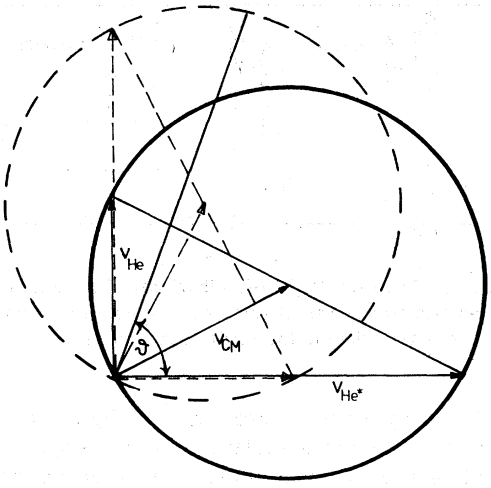

FIG. 4. Velocity vector, or Newton, diagram for He*–He scattering. v_{He^*} and v_{He} are the velocities of the excited- and ground-state beams, respectively. $v_{c.m.}$ is the velocity of the center of mass. For the diagram with the solid lines the ground-state beam energy is 16.5 meV, and the excited-state beam energy 62 meV. For the dashed-lined diagram the two values are reversed. This gives the same c.m. energy but different energies under some scattering angle.

shows the experimental results. They differ by up to a factor of 4 at some angles because of the different Jacobian transformation factors from the center of mass (c.m.) to lab-system conversion. After converting the two differential cross sections to the c.m. system, they should be identical, save for the velocity dependence of the detection probability. Figure 6 shows the c.m. distributions. They are identical within experimental error. This implies that the emission probability is independent of the kinetic energy in the 17–86 meV range. The same method will be used in future work to extend these measurements to higher kinetic energies.

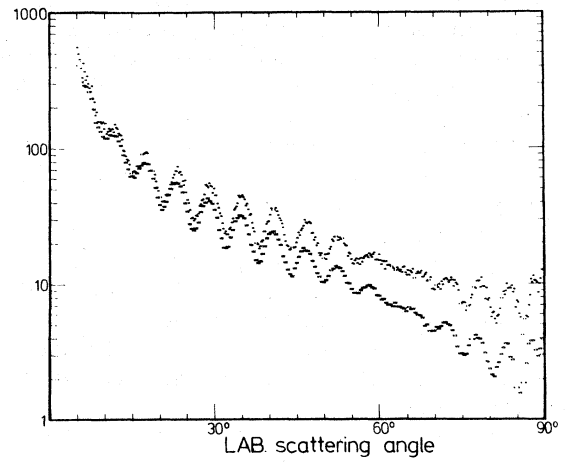

FIG. 5. Experimental data corresponding to the two Newton diagrams of Fig. 4. The data have been normalized at small scattering angles. There is a difference in intensity up to a factor of 4 at large scattering angles.

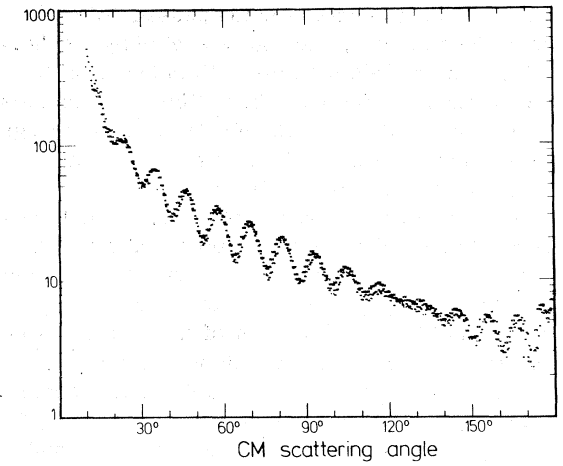

FIG. 6. Transformation of the data of Fig. 5 to the c.m. system. The results are identical within experimental error. This implies that the detection efficiency is independent of the kinetic energy of the He* atoms in the 18–86-meV kinetic energy range.

A stationary monitor detector (not shown in Fig. 2) is placed ~30° out of the plane of the two beams. It has a large viewing angle, and its high count rate is used to time normalize all data. The intensity of the metastable beam can be monitored by a secondary emission detector.

E. Data handling

The amplified pulses of the two detectors (moveable and monitor) are fed into two forward-backward counters, synchronized to the ground-state beam chopper. The total count rate of the two detectors, which is needed to calculate the He* beam profile and the statistical error, is stored in two other counters. A stepping motor rotates the detector. The digital information of its angular position if fed into a fifth counter. The timing and read out of the five counters and the operation of the stepping motor and of the high-voltage power supplies for the quenchlamps are controlled by a small hard-wired controller. The data of all five counters are punched on paper type and processed off-line.

Figure 7 shows an example of the primary data. Curve C gives the output of the monitor detector. The two steps are caused by increases of the measuring time to improve the signal to noise ratio. Curve A is the angular distribution, and is obtained by normalizing each data point with the reading of the monitor detector. Due to this normalization procedure, intensity drifts and fluctu-

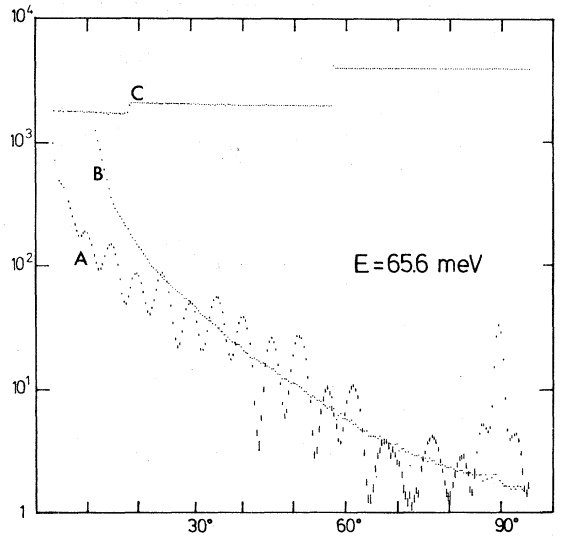

FIG. 7. Primary experimental data. Curve A gives the angular distribution, curve B is the far wing of the beam profile of the He* beam. Curve C is the reading of the monitor detector. The count time has been increased twice to improve the statistics. Each point of curves A and B has been separately normalized with the intensity of the monitor detector.

ations are compensated. Curve B is the He* beam profile. The error bars of curve A are calculated by the standard error propagation formula. The ordinate is the same for curves A and B. All angular distributions shown in Sec. II F have been measured twice and were only accepted if they agreed within experimental error.

F. Photon-induced artifacts

For the scattering of He($2\,^3S$)+He, a very narrow peak was always observed at $\theta_{lab}=90°$, as shown in Fig. 8. The ratio of the intensity at θ $=90°$ to that at some other angle was independent of nearly every experimental parameter (beam intensity, electron current and voltage, magnetic field, background and ground-state beam inlet pressure) so that it was concluded at first[16] that the 90° spike was not an experimental artifact. Only after it was impossible to produce a similar spike in a theoretical computation, a second detailed investigation revealed the following cause.

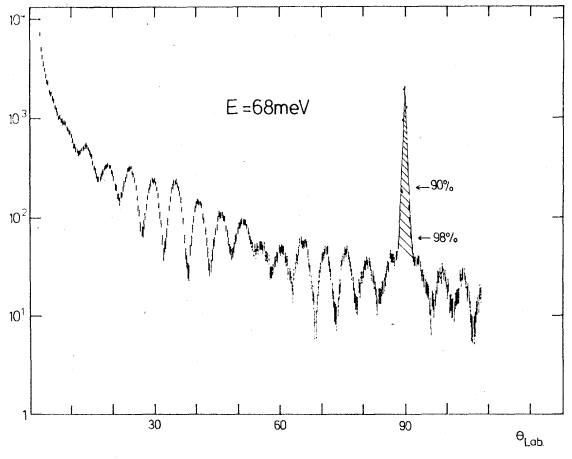

FIG. 8. Photon-induced spike near $\theta=90°$ for the scattering of He($2\,^3S$). The peak heights for 90% and 98% quenching efficiency are indicated.

There are always some photons from the He resonance transition ($2\,^1P \rightarrow 1\,^1S$, $E=21.21$ eV) in the beam. Because of the extremely large cross section for resonance absorption, they can be effectively trapped in a strong beam. Some of these photons will be absorbed in the scattering center by helium atoms of the ground-state beam. Most of them will decay back to the ground-state, but a fraction of 10^{-3} will make a transition to the metastable $2\,^1S$ state, and these atoms will be detected on the multiplier. This somewhat involved explanation was checked in two ways. (i) As the momentum transfer by the photon is negligible, the shape of the 90° spike should be given by the convolution of the angular profiles of the detector and the secondary beam. This turned out to be true. (ii) As $2\,^1S$ atoms are produced, they can be quenched by a quenchlamp after the scattering center. And the 90° spike disappeared nearly completely after the installation of the second quenchlamp.

As indicated in Fig. 8, even a 98% quenching probability is not sufficient to reveal the true shape of the angular distribution around 90° lab. Therefore this portion was generally disregarded in the fitting procedure.

No such problems ocurred for He($2\,^1S$)+He, as this is a double-difference measurement (quenchlamp on-off, He beam on-off).

A similar peak at $\theta_{lab}=90°$ was observed by Martin *et al.*[18] and Haberland *et al.*[19] for He*+Ne scattering. An interpretation similar to that for He*-He was given, but turned out to be incorrect.[20]

In summary, in scattering studies with excited atoms any sharp peak at $\theta_{lab}=90°$ is very valuable for testing the resolution of the apparatus, but should be regarded with suspicion.

III. EXPERIMENTAL RESULTS AND DATA ANALYSIS

Figures 9 and 10 show the measured distributions. Both distributions have been published earlier in brief communications.[21,22] The solid lines have been calculated from the potentials given below. For each point the statistical error bar is given, but it is usually too small to be resolvable on the scale of the figure. The regular oscillations are mainly due to nuclear symmetry,

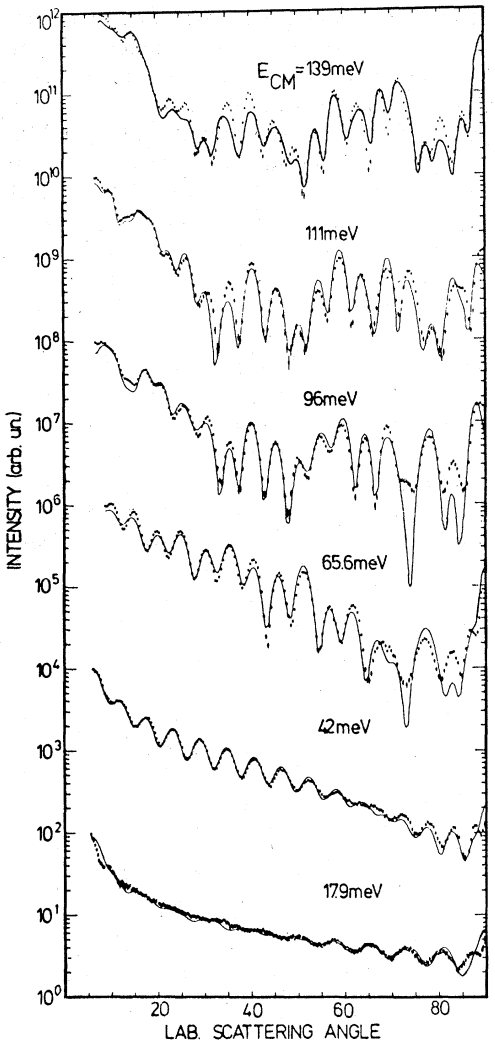

FIG. 9. Experimental angular distributions for He($2\,^1S$) + He. The solid lines have been calculated by the determined potential. The regular oscillations are due to symmetry oscillations. They are partially damped at the two lowest kinetic energies because of a crossing of the long-range potentials.

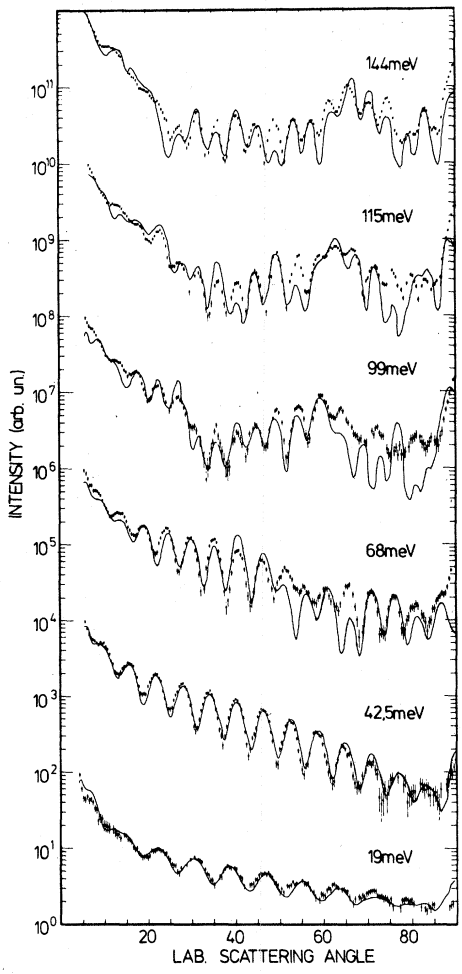

FIG. 10. Experimental angular distributions and fit for He($2\,^3S$) + He.

as discussed below.

For the fitting process, flexible piecewise analytical potentials are assumed, and the Schrödinger equation solved numerically. The differential cross section is calculated, transformed into the lab system, and averaged over experimental resolution. As it is very computer-time consuming to handle the velocity smearing properly, the average over the scattering angle is increased appropriately in order to incorporate the effect of the finite velocity resolution. The parameters of the analytical potentials are determined by the Marquardt nonlinear least-squares procedure.

The Marquardt routine can only find the best coefficients for some given analytical expression. To obtain a convenient analytical expression, the influence of the potential on specific parts of the angular distribution was analyzed by routinely calculating its "quantal deflection function," which is discussed in more detail in Sec. V.

The fitting procedure always starts with the lowest-energy result. When an acceptable fit is obtained, the differential cross section at the next-higher kinetic energy is calculated. Generally, one has to adjust the potential a bit until both angular distributions are fitted. Then the data of the next-higher kinetic energy are taken into account. This time-consuming iterative procedure is continued until one potential fits all the differential cross sections.

It would obviously be very desirable to have an inversion procedure from the differential cross section directly to the potential. As discussed in Sec. V, up to eight impact parameters can lead

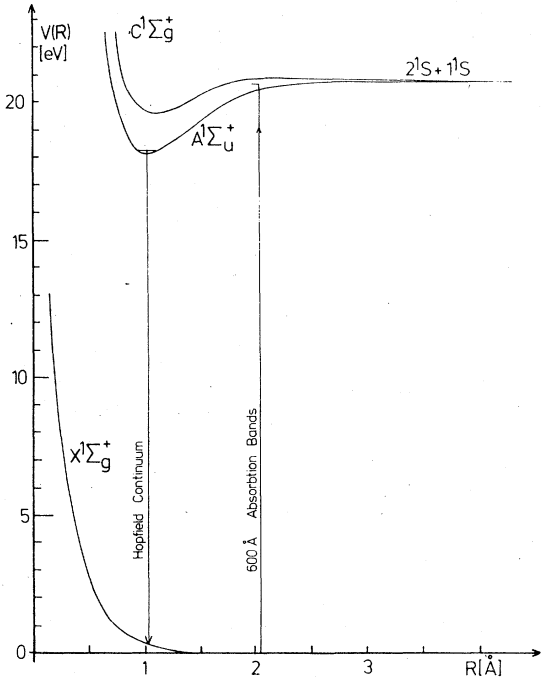

FIG. 11. Lowest singlet potential curves of the He_2 molecule.

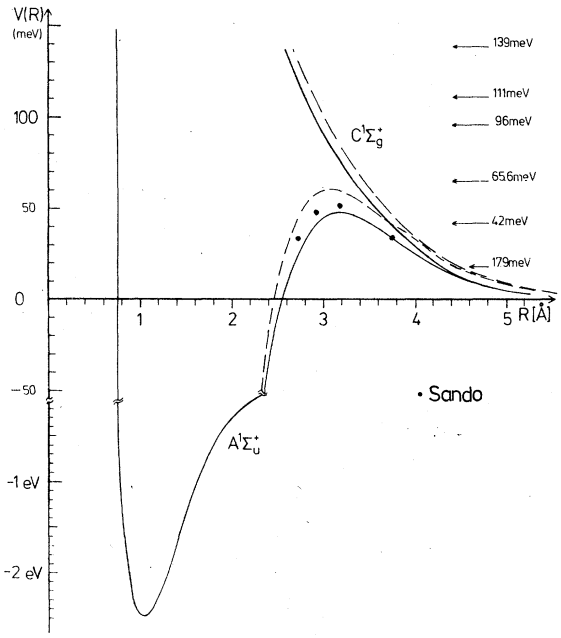

FIG. 12. Enlarged part of the excited state potentials shown in Fig. 11. The solid lines for $R > 2.4$ Å have been determined from the differential cross sections. The dashed lines are from the calculation by Guberman and Goddard. The deep attractive part of the potential and the solid points had been determined earlier by Sando. The apparent break in the curve comes from the change of scale at − 50 meV. The horizontal arrows give the collision energies used in this experiment.

to one scattering angle and the differential cross sections are strongly influenced by orbiting collisions, and no known inversion procedure can handle these situations. For energies well below 50 meV, when orbiting is no longer important, Siska[41] has developed an inversion procedure.

Of course, the question of accuracy remains. From our experience we can say that from data over a narrow energy range (say a factor of 2) no accurate potential can be obtained. But a measurement of the differential cross section every 30 meV over a factor of 5–8 in energy is usually sufficient to determine an accurate potential for the energy range covered. In Sec. IV, the error estimates for the positions and heights of the potential maxima are given. These estimates were obtained by keeping the parameters of the maxima fixed while optimizing the other parameters of the potentials.

The potentials obtained are shown in Figs. 11, 12, and 14, their analytical form is given in Tables II and IV, and numerical values are given in Tables III and V. No serious attempt was made to keep the number of free parameters small. It is obvious from Figs. 9 and 10 that especially the triplet results can still be improved.

IV. DISCUSSION OF THE POTENTIALS

The unusual shape of the excited He_2 potentials has been discussed by many authors,[10,11] These potentials are also called excimer potentials, and the corresponding states for the heavier rare gases have been used as energy storage reservoirs for the rare-gas excimer lasers.[23] An excimer state corresponds by definition to an excited attractive molecular potential having a dissociation ground state.

Figure 11 shows the lowest singlet potentials. The ground state is purely repulsive, save for a 1-meV Van der Waals minimum at 3 Å which is too small to be seen on this scale. The asymptotically degenerate excited state splits into a g and u component for smaller R. Both potentials have a very shallow (~1 meV) Van der Waals minimum at $R > 6$ Å, and a very deep (~2 eV) inner minimum separated by an intermediate maximum.

Some spectroscopic information on the inner minima is available from the analysis of the Hopfield emission continuum and the famous 600-Å emission and absorption bands.[8,24]

The splitting of the two excited curves can easily be understood. Asymptotically one prepares one beam with electronically excited atoms (A) and the other one with ground-state atoms (B). Consequently the electronic wave function can be written

$$\phi_1(A)\phi_0(B), \qquad (1)$$

TABLE II. Analytical form of the singlet potentials. Units are meV and Å.

Ungerade potential $A^1\Sigma_u^+$

Morse potential (from Sando[24])
$V(R) = V^M(R) = 3061.1\,[\exp - \{2.0407(R - 1.0399)\} - 1]^2 - 2494.1$ for $0 \le R < 1.693\,44$
Modified Morse (fits Sandos numerical values)
$V(R) = V^M(R) - 117.05\{\sin[(\pi/0.84672)(R - 2.1168)] + 1\}$ for $1.693\,44 \le R < 2.05$
1. Spline

$$V(R) = -251.016 + (R - 2.05)\{398.495 + (R - 2.75)[-811.622 + 549.183(R - 2.05)]\}$$

for $2.05 \le R < 2.75$

Parabola
$V(R) = 47.377 - 130.03(3.137 - R)^2$ for $2.75 \le R < 3.137$
2. Spline

$$V(R) = 47.377 + (R - 3.137)\{-25.32 + (R - 3.9)[-34.236 + 31.291(R - 3.137)]\}$$

Modified expotential for $3.137 \le R < 3.9$

$$V(R) = 193\,66.84\exp\left(-\left\{1.3650 + 0.4408\exp\left[-\left(\frac{R - 2.627}{0.9134}\right)^2\right]\right\}R - 0.0636R^2\right) \text{ for } 3.9 \le R < \infty$$

Gerade potential $C^1\Sigma_g^+$

Modified expotential
$V(R) = 63\,860.33\exp(-AR - 0.0570R^2)$
with $A = 1.6385 + 0.07\exp[-\{(R - 2.5)/0.3\}^2] + 0.566\exp\{-[(R - 2.22)/1.2075]^2\}$ for $2.7 \le R < \infty$

where $\phi_1(A)$ means that atom A is in the excited state and $\phi_0(B)$ means that atom B is in the ground state. As the Hamiltonian is invariant with respect to interchange of atom A and B,

$$\phi_1(B)\phi_0(A) \tag{2}$$

is also a possible wave function. A linear combination will then give the correct asymptotic eigenfunction

$$\chi^{g,u}(R \to \infty) \sim \phi_1(A)\phi_0(B) \pm \phi_1(B)\phi_0(A)\,, \tag{3}$$

where g (gerade) stands for the plus sign and u (ungerade) for the minus sign. The asymptotically prepared states are not eigenstates of the Hamiltonian when the atoms are closer together, but two new states, one with u, the other with g symmetry. Within the Born-Oppenheimer approximation, the total interaction is averaged over the electronic wave functions for fixed R. As one averages over different electronic wave functions, one obtains different interaction potentials V^g and V^u. Within the Born-Oppenheimer approximation the potential does not depend on the mass of the heavy particles, so that the potentials for ^{4}He^{4}He, ^{4}He^{3}He, and ^{3}He^{3}He are identical. There is no coupling between the two states, as χ^g and χ^u possess different symmetry properties, and any matrix element of the form $\langle \chi^g | T | \chi_u \rangle$ has to be zero for collision partners of equal mass.

Obviously, the two potentials V_g and V_u can also be written

$$V_g = V_0 + V_1, \quad V_u = V_0 - V_1\,. \tag{4}$$

At the end of this section (see Fig. 13) it will be shown that the difference potential $V_g - V_u = 2V_1$ calculated by Guberman and Goddard agrees with the experimentally determined one within the experimental accuracy. The calculated average po-

TABLE III. Numerical values for the singlet potentials $V_g = C^1\Sigma_g^+$ and $V_u = A^1\Sigma_u^+$.

R (Å)	V_g (meV)	V_u (meV)
0.5		9867
0.75		−501
1.00		−2472
Min (1.05)		−2492
1.25		−2122
1.50		−1359
1.75		−704
2.00		−303
2.25		−101
2.50	163	−82.0
2.80	109	32.6
3.00	90.1	44.9
Max (3.15)	77.2	47.4
3.20	73.4	47.2
3.40	59.8	44.1
3.60	48.0	38.4
3.80	37.5	31.5
4.00	28.2	24.7
4.20	20.3	18.5
4.40	14.2	13.3
4.60	9.6	9.2
4.80	6.4	6.3
5.00	4.1	4.2
5.25	2.4	2.6

TABLE IV. Analytical form of the triplet potentials. Units are meV and Å.

Ungerade potential $V_u\, a^3\Sigma_u^+$
Morse potential (Ginter)
$V(R) = 2611.2[\exp\{-2.1492(R-1.045)\}-1]^2 - 1947.2$ for $0 \le R < 1.203$
Spline potential
$V(R) = -1731.974 + (R-1.203)\{2688.072 + (R-1.77)[662.348 - (R-1.203)6077.531]\}$ for $1.203 \le R < 1.77$
R^4 potential
$V(R) = 57 - 265(2.77 - R)^4$
Spline potential
$V(R) = 57 + (R-2.77)\{-36.914 + (R-3.86)[-32.708 + 32.523\,(R-2.77)]\}$ for $2.77 \le R < 3.86$
Modified exponential
$V(R) = 9081.6\exp[-(1.4771 - 0.1929\exp\{-[(R-3.1)/5.0]^2\})R - R^2 \cdot 0.0887]$ for $3.86 \le R < \infty$
Gerade potential $V_g\, c^3\Sigma_g^+$
Spline function
$V(R) = 144.676 + (R-2.6)\{-108.35 + (R-3.6)[2.070 + 29.76\cdot(R-2.6)]\}$ for $2.6 \le R < 3.6$
Modified exponential
$V(R) = 41\,454.1\exp\left(-\left\{1.7116 + 0.3650\exp\left[-\left(\frac{R-2.3}{0.6036}\right)^2\right]\right\}R - R^2 \cdot 0.0668\right)$ for $3.6 \le R < \infty$

tential $\frac{1}{2}(V_g + V_u) = V_0$, on the other hand, is too large.

A. Singlet potentials

The analytical form of the potentials used is given in Table II. For large internuclear distances R the analytical form of the potential was taken as

$$V(R) = A\exp[-B(R)R - CR^2]\,,$$

where $B(R)$ is given by a constant plus an additive Gaussian. This allows a local and smooth variation of the exponent. The very-long-range Van der Waals interaction was neglected, as it did not have a noticeable effect on the angular distribution, save for backward scattering ($\theta \approx 180°$) at the lowest kinetic energy. If the minimum distance was allowed to vary in the automatic fit routine, it was iterated to distances larger than 6 Å.

TABLE V. Numerical values for the triplet potentials $V_g = c^3\Sigma_g^+$ and $V_u = a^3\Sigma_u^+$.

R (Å)	V_g (meV)	V_u (meV)
0.5		10990
0.75		98
1.00		−1920
Min (1.05)		−1947
1.25		−1615
1.50		−842
1.75		−232
2.00		−36.1
2.25		37.6
2.40		52.0
2.60	144.7	56.8
Max (2.75)	127.6	57.0
3.00	97.9	53.5
3.20	74.8	46.5
3.40	53.8	37.3
3.60	36.3	27.6
3.80	23.6	18.9
4.00	15.1	12.6
4.20	9.6	8.3
4.40	6.1	5.4
4.60	3.8	3.5
4.80	2.4	2.2
5.00	1.5	1.4
5.25	0.82	0.78

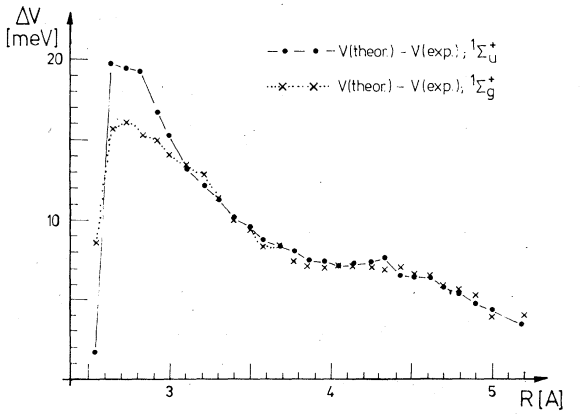

FIG. 14. Difference of the calculated and experimental results for the first excited singlet state of the He_2 molecule. Within experimental error the two curves are identical for $R > 3$ Å, implying that the neglected part of the correlation error is independent of the g/u symmetry and given directly by this figure (for $R \gtrsim 3$ Å).

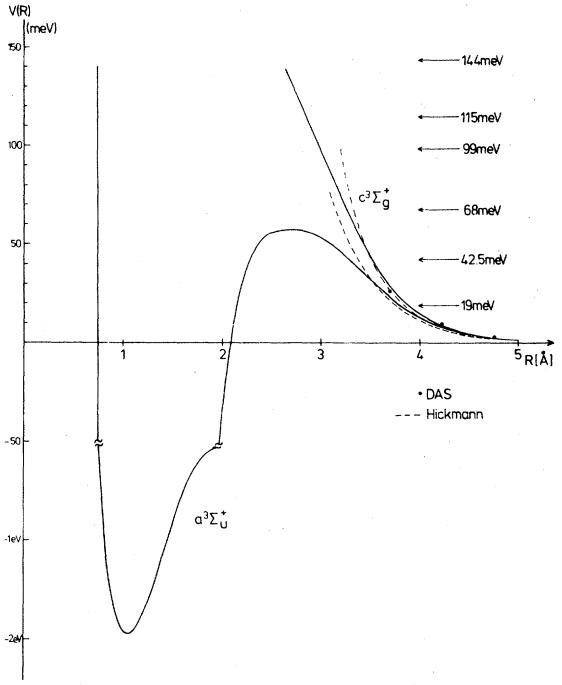

FIG. 14. Potential energy curves for He($2\,^3S$) + He.

Together with the known Van der Waals constant[17,25] this gives a well depth smaller than 0.5 meV. Although the Van der Waals potentials have only a very small influence on the angular distributions, they have a very significant effect on the velocity distributions in the metastable helium beam,[13] because the relative velocities of the He* atoms in the beam are much lower than the collision energies.

The small-R part of the potential maximum was represented by a parabola.

The height of the potential maximum is 47^{+2}_{-1} meV at an internuclear distance of 3.1 ± 0.05 Å. The interpolation at both sides of the parabola was performed by two cubic spline functions. The minimum of the $A\,^1\Sigma_u^+$ potential was described by a Morse function, which was proposed by Sando.[24] It reproduces Ginter's[26] spectroscopic molecular constants. Sando also gives some numerical values, which were approximated for $1.6 \leq R \leq 3.05$ Å by subtracting a properly scaled sine function from this potential. Figure 11 shows the potential used. The $C\,^1\Sigma_g^+$ potential also has a minimum at small R, but the potential maximum is too high to be overcome at our kinetic energies.

Figure 12 shows the long-range part of the potential in more detail. The apparent break in the curve is caused by the change of scale near −50 meV. The kinetic energies used in these experiments are given by the horizontal arrows. Our data are sensitive only to the long-range part of the potential between −50 and 130 meV. The numerical values obtained by Sando are given as dots in Fig. 12.

The dashed line gives the potential calculated by Guberman and Goddard with the generalized valence bond (GVB) method, which always gives rigorous upper bounds to the exact result.[11]

Figure 13 shows the difference between the experimental and calculated results. It is rather remarkable that for $R > 3$ Å this difference is the same, independent of the g-u symmetry of the potential. This implies that the experimental and theoretical difference potentials [see Eq. (4)] agree with each other for $R > 3.0$ Å within 1–2 meV, while the average potentials disagree by 5–20 meV. Guberman and Goddard propose a 10%–20% reduction of their results to account for neglected parts of the correlation energy, but this reduction is sufficient only between 3.2 and 4.0 Å.

They calculate their results for $R \to \infty$ to an absolute accuracy of ~0.5%. As the absolute value of the difference potential has to go to zero asymptotically, it should have been calculated very accurately indeed. This implies that our difference potential is accurate to 1 or 2 meV. This is also the experience we have gained from the fitting procedure. As the differential cross sections are very sensitive not only to the difference but also to the mean potential [see Eq. (4)], we believe that our singlet potentials are accurate to 1 or 2 meV. If this argument is correct, Fig. 13 will give directly the R dependence of the neglected part of the correlation energy.

B. Triplet potentials

The analytical form of the triplet potentials is given in Table IV. The long-range parts are given again by the modified exponentials used for the singlet potentials. The height of the potential maximum is 57^{+5}_{-3} meV at an internuclear distance of 2.77 ± 0.1 Å. The small-R part of the potential maximum could not be fitted by a parabola as in the singlet case; an R^4 functional dependence was found to be more adequate. The deep chemical well at 1.045 Å was represented by a Morse function, which reproduces Ginters spectroscopic result.[26]

The very-long-range part of the potential has been calculated by Das[27] in a multiconfiguration self-consistent-field (S.C.F) computation. He obtains a Van der Waals minimum at ~7 Å with a well depth of 0.16 meV, which is consistent with our results. The dotted lines have been deter-

mined by Hickman and Lane[28] from thermal-diffusion and exchange measurements. The agreement is satisfactory below 40 meV. Their data were limited to this energy range. The earlier attempts to obtain the triplet potentials from bulk experiments have been reviewed by Fugol'.[29]

C. Differences and similarities between the singlet and triplet potentials

All four potentials determined from the differential cross sections are shown together in Fig. 15. The repulsive wall is independent of the spin state. Each of the two ungerade potentials has an intermediate maximum, which is *not* due to a curve crossing. The gerade potentials are purely repulsive within our energy range, but also have maxima which are curve-crossing induced, as discussed in detail by many authors.[10,11]

Guberman and Goddard[11] point out that the long-range part of the potentials should have a simple interpretation, because the small 1*s* orbital of the ground-state atom is in effect a local probe of the large 2*s* orbital of the excited atom. The two authors show that the potential should vary roughly as the square of the amplitude of the 2*s* orbital at the nucleus of the ground-state atom. Figure 16 shows the radial one-electron-charge density as calculated by Winkler and Porter[30] for the two spin states.

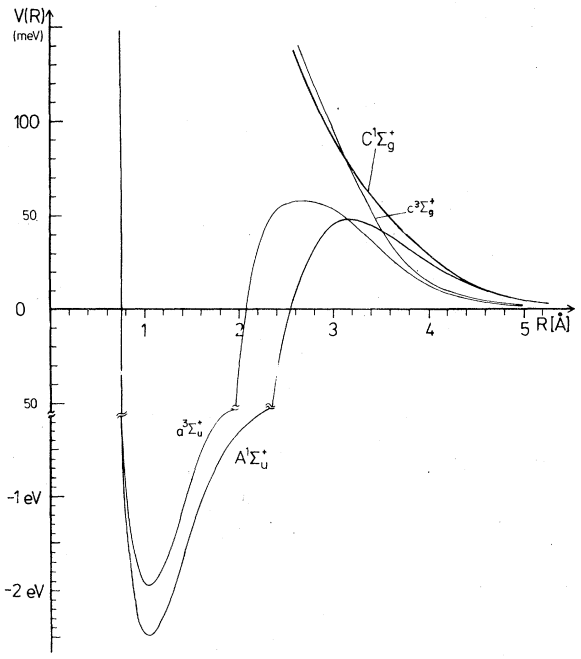

FIG. 15. Comparison of the helium excimer potentials determined in this work. The triplet potentials have a shorter range.

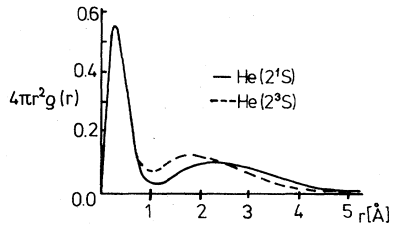

FIG. 16. Radial electron densities for the two excited He states as calculated by Winkler and Porter.

The triplet orbital has a smaller diameter than the singlet orbital; consequently, the maxima of of the triplet potentials are at smaller distances. If one shifts the triplet charge density by 0.62 Å, it overlaps with the singlet charge density at 5 Å, as shown in Fig. 17(a). Shifting the triplet potentials by the same amount, one obtains the results of Fig. 17(b) and 17(c). The potentials and the charge density show roughly the same behavior, as predicted by Guberman and Goddard.

V. DISCUSSION OF THE INTERFERENCE STRUCTURE

The interference structure of the differential cross sections is more complicated than usual in atom-atom scattering—first, because two potentials contribute coherently, whose shapes are different from the usual ground-state potentials, and second, because of the identical nu-

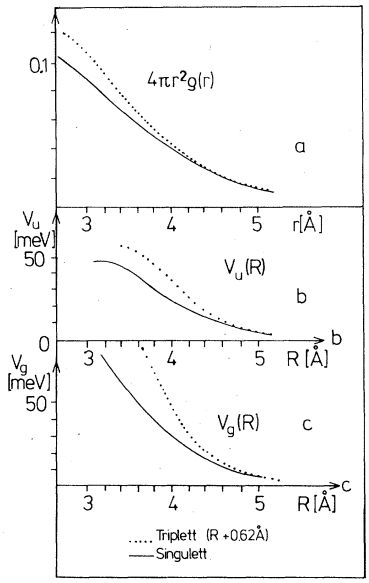

FIG. 17. Long-range parts of (a) the radial electron density, (b) the ungerade potentials, and the (c) gerade potentials. The triplet scale has been shifted by 0.62 Å. As discussed in the text, this figure proves the remark of Guberman and Goddard that for large R the small $1s^2$ charge density of the ground-state atoms is essentially a local probe of the diffuse 2*s* orbital.

clei. The potential does not depend on the different isotopes of the helium atom, as discussed in Sec. IV. The total scattering amplitude, on the other hand, depends very strongly on it. For the scattering of distinguishable particles, e.g., ^{4}He + ^{3}He, it becomes

$$f(\theta) = \tfrac{1}{2}[f_g(\theta) + f_u(\theta)] \,. \tag{5}$$

For indistinguishable particles this has to be symmetrized appropriately. The ^{4}He nucleus is a boson, and therefore the total wave function does not change sign when interchanging the nuclei. Therefore, the symmetrized scattering amplitude is given by

$$f(\theta) = \tfrac{1}{2}[f_g(\theta) + f_g(\pi - \theta) + f_u(\theta) - f_u(\pi - \theta)] \,. \tag{6}$$

The amplitude f_u is antisymmetric with respect to interchange of the nuclei, which is a direct reflection of the symmetry property of the corresponding electronic wave function. The minus sign in Eq. (6) destroys the symmetry of the differential cross section around $\theta = 90°$, which one has for the scattering of identical particles on *one* potential curve. The symmetrized scattering amplitude can be split up into a direct and an exchange contribution, as shown graphically in Fig. 18.

The amplitudes in Eq. (6) have been calculated by a numerical integration of the radial Schrödinger equation, although the WKB approximation is still reasonably good. Within the WKB approximation, each of the scattering amplitudes can be written

$$f(\theta) = \sigma_{cl}(\theta)^{1/2} \exp[i(2\eta - l\theta)] \,, \tag{7}$$

where σ_{cl} is the classical cross section, η and l are the radial phase shift and orbital angular momentum, respectively, giving the classical scattering angle θ. The term $-l\theta$ can be interpreted as "orbital phase shift."

The influence of the symmetrization can easily be studied by calculating the differential cross

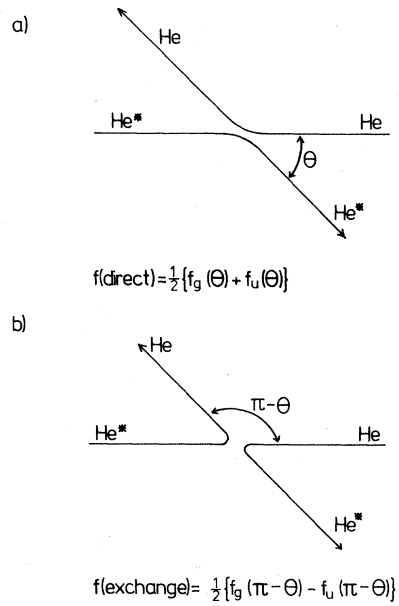

FIG. 18. Direct and exchange contribution to the total scattering amplitude [see Eqs. (5) and (6)].

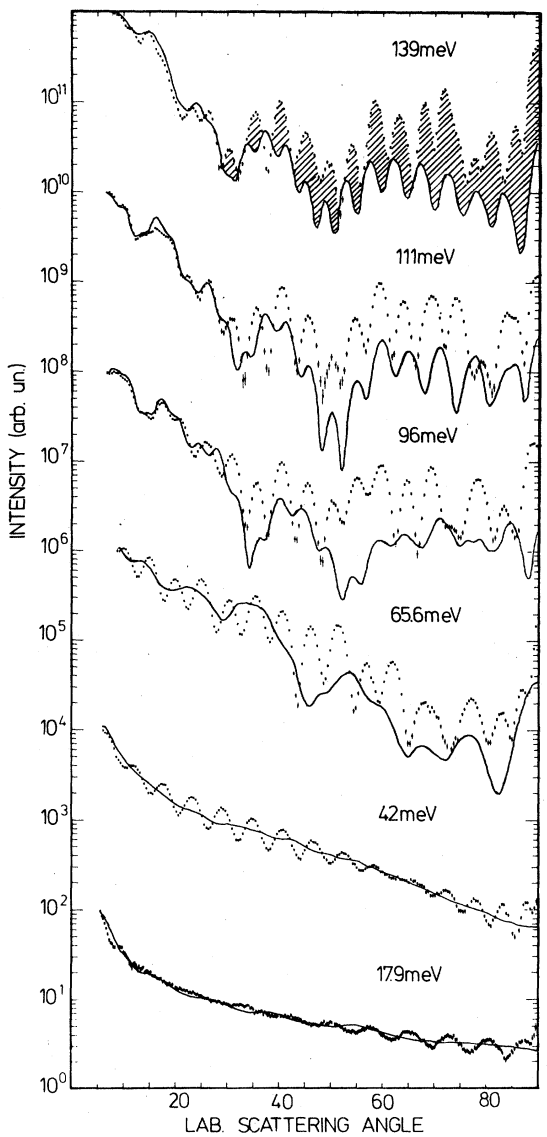

FIG. 19. Calculated cross section for He($2\,^1S$) + He assuming distinguishable particles. At low energy the regular oscillations are absent. The large effect of the exchange contribution can be seen at high energies. It is given by the shaded portions at the 139-meV measurement. The influence of the symmetrization is much less dramatic for the total cross sections (see Figs. 23, 24).

sections assuming distinguishable particles [Eq. (5)]. Figure 19 shows the results. The regular oscillations at lower energies are completely absent, so they must be due to nuclear symmetry. For the higher energies the peak at 90° is much smaller though still present, and the intensity at large angles is markedly decreased because of the loss of the exchange contribution. This is indicated by the hatched area of the 139-meV curve in Fig. 19.

At low kinetic energies, only the long-range part of the potentials is probed. For the singlet case the splitting of the potentials becomes very small as the two singlet potentials cross each other at $R = 4.88$ Å. Therefore, the difference of the scattering amplitudes will also be very small, i.e., $f_g - f_u \approx 0$. Inserting this into Eq. (6), one obtains the result that the symmetrized and unsymmetrized scattering amplitudes are identical for $V_g = V_u$. As this is a very good approximation for $He(2\,^1S) + He$ at large R, the symmetry oscillations are partially washed out at the two lowest energies (see Fig. 9).

The discussion of the oscillations in ground-state atom-atom scattering relies heavily on the classical deflection function, which can be calculated by a simple WKB type of integral if the potential is known. The classical deflection function is related to the phase shift via the well-known semiclassical relation

$$\theta(l) = 2\frac{d\eta}{dl} \tag{8}$$

assuming the angular momentum l to be a continuous variable. For the He*-He scattering the phase shifts are calculated quantum mechanically, and one has their values only for integer l. It has proved very convenient[31] to define a "quantal deflection function"[32] as

$$\theta(l + \tfrac{1}{2}) = 2(\eta_{l+1} - \eta_l) \ . \tag{9}$$

The phase shifts are calculated only modulo 2π, but the variation from one l to the next is rarely larger than 2π, so this does not present a big problem. With a little imagination and experience one can always draw a smooth curve.

Figure 20 shows the quantal deflection function for the 42-meV measurement. It shows the behavior expected for the scattering from a purely repulsive wall. The classical deflection function would give $\theta(l = 0) = \pi$ and it is surprising how close to this a value is attained. The deflection functions in Fig. 20 are very nearly linear, save for the largest l values. If they are linear one can show from Eq. (7) that the wavelength of the symmetry oscillations should be

$$\Delta\theta_{sym} = 2\pi/[l(\theta) + l(\pi - \theta)] \ , \tag{10}$$

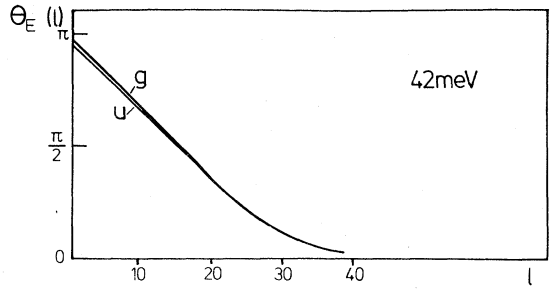

FIG. 20. Quantal deflection functions [see Eq. (9)] for the $He(2\,^1S) + He$ cross section at 42 meV.

where $l(\theta)$ is the orbital angular momentum corresponding to the classical scattering angle θ [via Eq. (8)]. If θ is a linear function of l, one can write

$$l(\theta) = l(\tfrac{1}{2}\pi) - \Delta l, \quad l(\pi - \theta) = l(\tfrac{1}{2}\pi) + \Delta l \ .$$

This gives for the wavelength of the symmetry oscillations

$$\Delta\theta_{sym} = \pi/l(\tfrac{1}{2}\pi) \ ,$$

which is independent of the scattering angle and therefore explains the very regular interference patterns at low kinetic energies. From Fig. 20 one has $l(\frac{1}{2}\pi) = 16$, which gives $\Delta\theta_{sym} = 11.2°$, in exact agreement with the 42-meV angular distributions of Fig. 9. Note that $\Delta\theta$ is given in the c.m. system, while Fig. 9 gives the data in the lab system ($\theta_{c.m.} = 2\theta_{lab}$).

Figure 21 shows the deflection functions calculated for three higher kinetic energies. For the gerade potentials one still gets the same monotonic behavior as at lower energies, but dramatic differences can be seen for the deflection functions for the ungerade potential V_u, because the kinetic energy of the particles is now higher than the potential barrier and spiral scattering (or orbiting) will occur in the very deep inner well. The deep minima in the deflection function result from orbiting. The maxima in the deflection function lead to rainbow scattering. The structure on the maxima comes from orbiting resonances.

Figure 22 shows schematically a deflection function from Fig. 21, taking into account nuclear symmetry. The dashed curves are from the exchange contribution and are obtained from the solid curves by replacing θ by $\pi - \theta$. Altogether one has four different types of oscillations, and it would have been nearly hopeless trying to disentangle their different and interfering contributions to the differential cross sections without the use of the deflection functions. One has the following types of oscillations:

(i) symmetry oscillations; because the nuclei

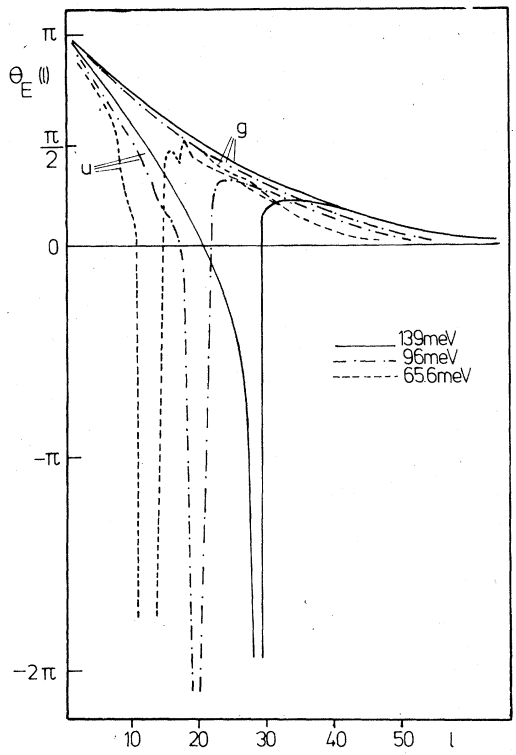

FIG. 21. Quantal deflection functions for He($2\,^1S$) + He at three higher kinetic energies. Orbiting occurs in the deep attractive well of the potentials. The structure on the maximum for $E = 65.6$ meV comes from barrier penetration effects.

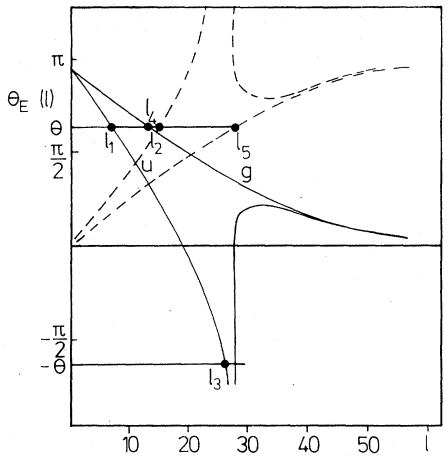

FIG. 22. A deflection function as in Fig. 21, including the effect of nuclear symmetry.

are indistinguishable. According to (10), their wavelength is roughly

$$\Delta\theta_{sym} = 2\pi/[l(\theta) + l(\pi - \theta)] = 4\pi/[(l_1 + l_2) + (l_4 + l_5)], \tag{10a}$$

where the l_i are defined in Fig. 22.

(ii) g-u oscillations; loosely speaking, half of the incident flux is scattered from V_u the other half from V_g. These two contributions add coherently at the detector. The wavelength of the oscillations is approximately

$$\Delta\theta_{g-u} = 2\pi/[l_g - l_u] = 2\pi/[l_1 - l_2]. \tag{11}$$

Note the minus sign in this equation. As can be seen from Fig. 21 and verified in Fig. 9, the wavelength of the oscillations increases with increasing scattering angle. The calculated wavelength is again in good agreement with the experimental results.

(iii) Orbiting oscillations; their approximate wavelength can be read off Fig. 21:

$$\Delta\theta_{orb} = 2\pi/[l(\theta) + l(-\theta)] = 2\pi/[l_1 + l_3]. \tag{12}$$

The trajectories that go round the origin (once or several times) have only a small effect on the differential cross section because of the large slope of the deflection function in the orbiting region. For the higher energies, symmetry and orbiting oscillations have roughly the same wavelength.

(iv) rainbow oscillations; the rainbow peaks are completely buried under the other oscillations. Their position could only be identified in calculations, which assumed the scattering to occur only from the ungerade potential V_u.

The following conclusions can now be drawn from this analysis: (a) At the two lowest kinetic energies only symmetry oscillations are present. (b) For the higher energies symmetry and orbiting oscillations have roughly the same wavelength, so that the fast oscillations are a superposition of these two contributions. (c) Because of the minus sign in the denominator in Eq. (11), the g-u oscillations are much slower. They give rise to the slow modulation of the faster oscillations. The wavelength of all these oscillations decreases with increasing collision energy. Similar potentials and the same symmetries hold for the scattering of He^+ from He. At ~500 eV the g-u oscillations are dominant, and it is difficult to resolve the symmetry oscillations.[33]

VI. TOTAL CROSS SECTIONS

The total cross sections calculated from the potentials in Tables II and IV are shown in Figs. 23 and 24. The solid lines are for identical particles, while the dotted lines have been calculated assuming distinguishable particles. For He($2\,^3S$) + He the experimental data of Trujillo[34] are included in Fig. 24. The total cross section for He($2\,^1S$) is roughly 40 Å^2 larger than that for He($2\,^3S$). For energies below the barrier

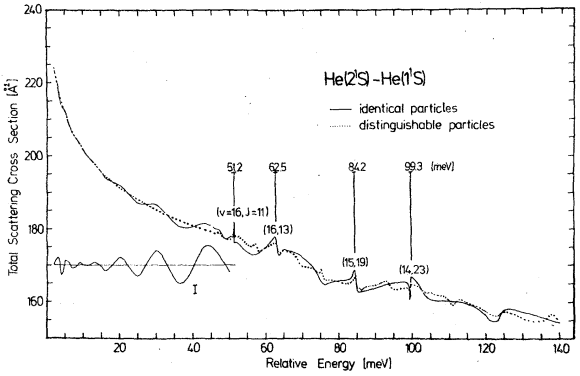

FIG. 23. Total cross sections calculated for He($2\,^1S$) + He. The sharp structures are shape resonances classified according to their energy and vibrational (v) and rotational (J) quantum number. The effect of the symmetrization is rather small.

heights the cross sections for distinguishable particles can be well approximated by

$Q = Av^{-B}$ Å^2

	He($2\,^1S$)	He($2\,^3S$)
A	503	529
B	0.14	0.18

Usually the total cross sections at low energies are dominated by the Van der Waals interaction. But in the He*-He scattering this interaction is so small because of the large spatial extension of the He(2s) orbital that it will become dominant only at kinetic energies below roughly 1 meV. As seen in Fig. 16, the He* singlet orbital is larger and softer than the triplet orbital. Therefore the total singlet cross section is larger and depends less on the kinetic energy.

The oscillations below ~50 meV have to be symmetry oscillations as they vanish for distinguishable particles. They result from the interference

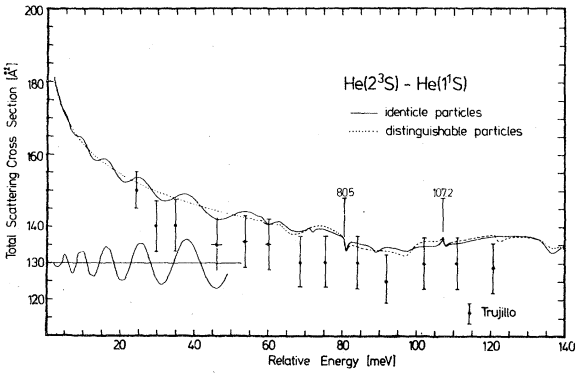

FIG. 24. Total cross sections for He($2\,^3S$) + He calculated from our potential and compared to the data of Trujillo. The agreement between the two independent determinations is good.

of collisions with large impact parameters, which are nearly forward scattered ($\theta \approx 0$), with energy transfer collisions at small impact parameters and $\theta \approx \pi$. The relative difference between the two cross sections is given by curve I (arbitrary scale). The position of the different maxima is nearly entirely given by the energy dependence of the S-wave phase shift, as shown elsewhere.[35]

The sharp structures above 50 meV are due to orbiting or shape resonances from the deep attractive well of V_u. All particles can tunnel through the maximum in V_u. The amplitude for finding a particle inside of the maximum will be resonantly enhanced if the kinetic energy matches the energy of a quasibound state of V_u. For energies much below the barrier height, the tunneling probability and therefore also the width of the resonance will be small, and could therefore only accidentally be detected using the grid used in calculating the curves for the total cross section. If the kinetic energy is only a bit smaller than the barrier height of the effective potential, the width of the resonance will become larger. They also cause the structure on the rainbow maxima of the deflection functions in Fig. 21. These resonances play a large role in the calculation of the 600-Å band[8,24] emitted by He($2\,^1S$) particles crossing the barrier. This spectrum and the resonances have been calculated by Sando[26] using his potential (V^M of Table II). The resonances can be classified according to their vibrational (v) and rotational (I) quantum number, which can be deduced from the inspection of the calculated wave functions. The cross section for light emission[1] is smaller than 10^{-19} cm^2, and was therefore neglected.

VII. EXCITATION-TRANSFER CROSS SECTION

In principle there is no way to measure the exchange process directly for ^{4}He* + ^{4}He scattering, as the particles are indistinguishable. But the cross section for metastability exchange can of course be calculated from the determined potentials assuming distinguishable particles. From Eq. (6) and Fig. 18 the amplitude of excitation transfer is

$$f_{ex} = f_g(\pi - \theta) - f_u(\pi - \theta) \ .$$

The expression for the total excitation-transfer cross section[1] becomes

$$\sigma_{trans} = \frac{\pi}{k^2} \sum_{l=0}^{\infty} (2l+1) \sin^2(\eta_l^g - \eta_l^u) \ , \qquad (13)$$

where $\eta_l^{g,u}$ is the lth phaseshift calculated from $V_{g,u}$. The transfer cross section is mainly determined by the difference potential. The cal-

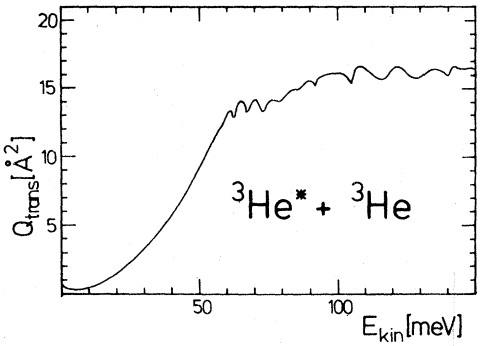

FIG. 25. Calculated total excitation-transfer cross section for ^{3}He($2\,^3S$) + ^{3}He assuming distinguishable particles.

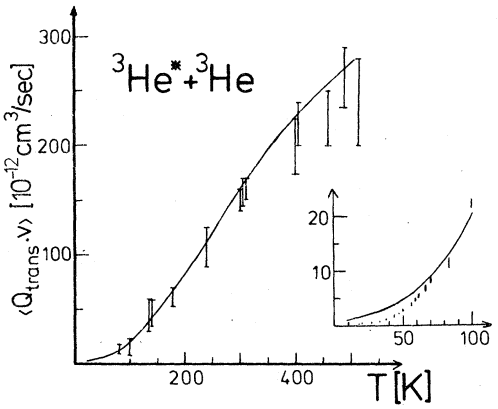

FIG. 26. Rate constant for excitation transfer obtained by averaging the cross section of Fig. 25. The experimental points are from two optical pumping experiments.

culated excitation-transfer cross section for ^{3}He($2\,^3S$) + ^{3}He is shown in Fig. 25 as a function of the kinetic energy. Because of the increasing splitting of the two potentials for smaller R, the cross section rises with kinetic energy. It starts to oscillate when the energy becomes larger than the barrier in the ungerade potential. The rate of excitation transfer (σ_{trans} times relative velocity, averaged over a Maxwellian distribution) is compared to experimental results in Fig. 26. The temperature dependence of these rates have been measured in two remarkable optical pumping experiments[36,37] in ^{3}He.

The ^{3}He nucleus has spin $\frac{1}{2}$, so that the hyperfine state can be different before and after a collision. This leads to a loss of coherence and a broader linewidth in the optical pumping experiments. The linewidth is measured as a function of temperature, and the rate of excitation transfer is obtained after an involved analysis. The agreement with the higher-temperature data of Colegrove *et al.*[36] is very good if the correction factor of $\frac{9}{4}$ is applied to their data, as proposed by Dupont-Roe *et al.*[38] The agreement is not so good with the lower-temperature results of Rosner and Pipkin[37] shown in the insert. This is probably due to the neglect of the Van der Waals interactions, which have only a negligible influence on the differential cross section. Barbé[42] has measured the excitation-transfer cross section at 4.2 °K, which corresponds to an average collision energy of ~0.5 meV. At this low energy the Van der Waals well should influence this cross section strongly.

Earlier theoretical calculations of excitation transfer have been performed for He* + He by Evans and Lane[43] and Hickman and Lane,[28] and for Ne* + Ne by Cohen and Schneider.[44]

VIII. SIMILAR TRANSFER PHENOMENA

There are many similar excitation-transfer phenomena: spin exchange ($K\uparrow + Cs\downarrow \rightarrow K\downarrow + Cs\uparrow$),[39] charge exchange[33] ($He^+ + He \rightarrow He + He^+$), or at much higher energies[40] neutron exchange ($^{12}C + {}^{13}C \rightarrow {}^{13}C + {}^{12}C$), or at even higher[40] energies π^- exchange ($p + n \rightarrow n + p$). Save for the last example where no local potential can be defined, there is a surprising similarity in the scattering phenomena and even in the language to describe them.

Note added in proof. The He*-He potentials have also recently been calculated by Peach.[45] The excitation transfer cross section has also been measured by Zhitnikov *et al.*[46]

ACKNOWLEDGMENTS

Generous financial support by the Deutsche Forschungsgemeinschaft is gratefully acknowledged.

[1]H. S. W. Massey, *Electronic and Ionic Impact Phenomena* (Clarendon, Oxford, 1971), Vol. III.
[2]W. R. Bennett, Jr., Appl. Opt. (Optical Maser Suppl.) 24 (1962).
[3]W. Happer, Rev. Mod. Phys. 44, 169 (1972).
[4]A. V. Phelps, Phys. Rev. 99, 1307 (1955).
[5]E. Illenberger and A. Niehaus, Z. Phys. B 20, 33 (1975), and references cited therein.
[6]R. D. Rundel and R. F. Stebbings, *Case Studies in Atomic Collision Physics*, edited by E. W. McDaniel and M. R. C. McDowell (North-Holland, Amsterdam, 1972).
[7]J. Wisdom, T. W. Hartquist, and N. F. Lane, Phys. Rev. B 14, 4205 (1976), and references cited therein.
[8]R. E. Huffman, Y. Tanaka, and J. C. Larabee, Appl. Opt. 2, 617 (1963).
[9]S. E. Harris, Appl. Phys. Lett. 31, 498 (1977).
[10]R. A. Buckingham and A. Dalgarno, Proc. R. Soc. London, Sec. A 213, 506 (1952).
[11]S. L. Guberman and W. A. Goddard III, Phys. Rev. A 12, 1203 (1975), and references cited therein.

[12]R. Campargue and A. Lebehot, *Proceedings of the Ninth International Symposium on Rarefied Gas Dynamics*, edited by M. Becker and M. Fiebig (DFVLR Press, Porz-Wahn, Germany, 1974), Vol. CII.
[13]B. Brutschy and H. Haberland, J. Phys. E 10, 90 (1977).
[14]R. D. Rundel, F. B. Dunning, and R. F. Stebbings, Rev. Sci. Instrum. 45, 116 (1974).
[15]R. K. B. Helbing, J. Chem. Phys. 48, 471 (1968).
[16]H. Haberland, B. Brutschy, and K. Schmidt, *Proceedings of the 9th International Conference on the Physics of Electronic and Atomic Collisions* (University of Washington, Seattle, 1975), p. 443.
[17]G. A. Victor and K. Sando, J. Chem. Phys. 55, 5421 (1971).
[18]D. W. Martin, T. Fukuyama, R. W. Gregor, R. M. Jordan, and P. E. Siska, J. Chem. Phys. 65, 3720 (1976).
[19]H. Haberland, P. Oesterlin, and K. Schmidt, J. Chem. Phys. 65, 3373 (1976).
[20]H. Haberland, P. Oesterlin, and K. Schmidt, Ber. D. Bunsen Gesellschaft 81, 184 (1977).
[21]B. Brutschy and H. Haberland, Phys. Rev. Lett. 38, 686 (1977).
[22]B. Brutschy and H. Haberland, Sixth International Symposium on Molecular Beams, Noordwijkerhout 1977, Abstracts p. 90.
[23]Ch. A. Brau, in *High-Power Lasers and Applications* edited by K.-L. Kompa and H. Walther (Springer, Berlin, 1978).
[24]K. M. Sando and A. Dalgarno, Mol. Phys. 20, 103 (1971); K. M. Sando, Mol. Phys. 21, 439 (1971); K. M. Sando, Mol. Phys. 23, 413 (1972), and references therein.
[25]K. L. Bell, A. Dalgarno, and A. E. Kingston, J. Phys. B 1, 18 (1968).
[26]M. L. Ginter, J. Chem. Phys. 42, 561 (1965); M. L. Ginter and C. M. Brown, J. Chem. Phys. 56, 672 (1972).
[27]G. Das, Phys. Rev. 11, 732 (1975).
[28]A. P. Hickman and N. F. Lane, Phys. Rev. A 10, 444 (1974).
[29]I. Ya. Fugol', Sov. Phys. Usp. 12, 182 (1969).
[30]P. Winkler and N. R. Porter, J. Chem. Phys. 61, 2038 (1974).
[31]H. Haberland and K. Schmidt, J. Phys. B 10, 695 (1977).
[32]N. K. Glendenning, Rev. Mod. Phys. 47, 659 (1975).
[33]W. Aberth, D. L. Lorents, R. P. Marchi, and F. T. Smith, Phys. Rev. Lett. 14, 776 (1965), and references cited therein; D. Dhuicq, J. Baudon, and M. Barat, J. Phys. B 6, L1 (1973).
[34]S. M. Trujillo, *Proceedings of the 9th International Conference on the Physics of Electronic and Atomic Collisions* (University of Washington, Seattle, 1975), Abstracts p. 437.
[35]K. Schmidt, Ph.D. thesis (Freiburg, 1976) (unpublished); B. Brutschy, Ph.D. thesis (Freiburg, 1976) (unpublished).
[36]F. D. Colegrove, L. D. Schearer, and C. K. Walters, Phys. Rev. 135, A353 (1964).
[37]S. D. Rosner and F. M. Pipkin, Phys. Rev. A 5, 1909 (1972).
[38]J. Dupont-Roc, M. Leduc, and F. Laloë, Phys. Rev. Lett. 27, 467 (1971).
[39]D. E. Pritchard and F. Y. Chu, Phys. Rev. A 2, 1932 (1970); A. Höh, H. Oertel, and A. Schultz, Z. Phys. 235, 20 (1970).
[40]W. von Oertzen and H. G. Bohlen, Phys. Rep. C 19, 1 (1975).
[41]P. Siska (private communication).
[42]R. Barbé, J. Phys. B 9, 995 (1976).
[43]S. A. Evans and N. F. Lane, Phys. Rev. 188, 268 (1969).
[44]J. S. Cohen and B. Schneider, Phys. Rev. A 11, 884 (1975).
[45]G. Peach, J. Phys. B 11, 2107 (1978).
[46]R. A. Zhitnikov, V. A. Kartoshkin, and G. V. Ulement'ev, *Sixth International Conference on Atomic Physics, Riga, 1978, Abstracts of Contributed Papers*, edited by E. Anderson, E. Kranlinya, and R. Peterkop (Physics Institute of the Latvian SSR Academy of Sciences, Nr. LAFI-1409), p. 198; R. A. Zhitnikov, V. A. Kartoshkin, G. V. Ulement'ev, and L. V. Usachëva, Sov. Phys. JETP 44, 924 (1976).